Mutual Coupling Analysis of Open-Ended Ridge and Ridge Gap Waveguide Radiating Elements in an Infinite Array Environment

Mutual Coupling Analysis of Open-Ended Ridge and Ridge Gap Waveguide Radiating Elements in an Infinite Array Environment

Yingqi Zhang, Artem R. Vilenskiy, Marianna V. Ivashina
Antenna Group, Dept. of Electrical Engineering, Chalmers University of Technology, 41296 Gothenburg, Sweden
yingqi@chalmers.se

***Abstract*— In this paper, we discuss mutual coupling effects in 2-D beam-steerable antenna arrays based on open-ended ridge and ridge gap waveguide radiating elements. Considering potential applications for beyond-5G systems in W-/D-band, the radiating elements are designed full-metal realizing a high radiation efficiency. Various decoupling structures based on electromagnetic soft surfaces are applied to suppress the surface waves over the array apertures. The infinite array approach is used to analyze antenna unit cells in an isosceles triangular lattice, which results in the active reflection coefficient over a scan and frequency range. The latter is used to extract the values of the mutual coupling coefficients between the elements. The analysis demonstrates the effect of decoupling structures realizing a steep drop of the mutual coupling magnitude (≤ -20 dB) for closely-spaced array elements. This results in a wideband ($\geq 20\%$) and wide-scan ($\geq 50^{o}$) element beam-steering performance.**

***Keywords*— array mutual coupling, array antenna, wideband array, ridge gap waveguide, wide-angle beam steering.**

I. Introduction

While beyond-5G future wireless communication proposes the W- (75-110 GHz) and D-band (110-170 GHz) as the promising operating frequency range, owing to a relatively low atmospheric absorption loss and centimeter-level positioning accuracy [1] [2], the study in phased array antennas (PAAs) for 100+ GHz is increasing in demand facing various technological challenges. To compensate for an increased material dissipation and free-space path loss at these frequencies, such PAA designs are required to be high-gain and high-efficient with wide-angle scanning capabilities.

State-of-the-art solutions mainly adopted Antenna-On-Chip (AoC) and System-in-Package (SiP) implementations to realize scalable active PAAs [3] [4]. However, at least 30-40% of radiation efficiency is typically lost due to high material loss. On the other hand, W-/D-band full-metal PAAs have been proposed recently demonstrating higher radiation efficiency ($\geq 50\%$) and potential wide-scan ability. [5]–[7]. More recently, we have demonstrated several full-metal PAAs based on the open-ended *ridge gap waveguide* (RGW) [8], [9]. In general, open-ended *ridge waveguide* (WG) PAAs have been widely applied for microwave frequency radar applications [10]. However, their hollow metal structure significantly increases manufacturing complexity at 100+ GHz frequencies. At the same time, the RGW-based architectures can resolve this problem owing to the inherently contactless design, with the wideband and wide-angle beam-steering performance being preserved.

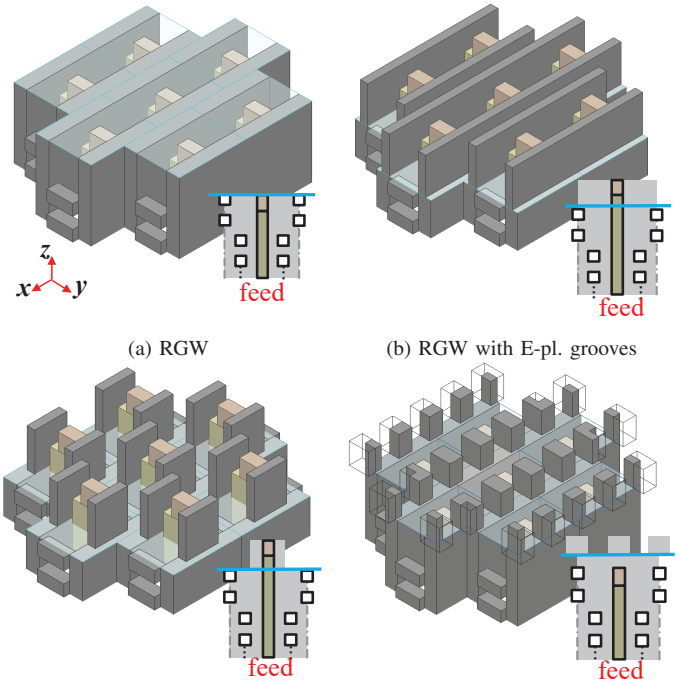

(a) RGW (b) RGW with E-pl. grooves

(c) RGW with E- & H-pl. grooves (d) RGW with AMC pins

Fig. 1. RGW array elements with various decoupling structures.

In this contribution, we further investigate the beam-steering performances of various open-ended WG and RGW array elements focusing on the elements mutual coupling analysis. In particular, we study the effects of adding fragments of electromagnetic soft surfaces (grooves, pins, and their combinations) in the array aperture that facilitates the adjacent elements decoupling and thus extends achievable beam-steering range.

II. Open-Ended WG and RGW Elements in an Infinite Array Environment

To cross-compare beam-steering capabilities and mutual coupling effects of various PAAs, the Ansys HFSS finite element method electromagnetic solver was used to analyze antenna unit cells (UCs) in the isosceles triangular array lattice

Table 1. Comparison of θ_{max} for various array elements, $|\Gamma| \leq -10$ dB over the 20% relative bandwidth (85–105 GHz) criterion.

	$\pm\theta_{max}$, **E-plane**	$\pm\theta_{max}$, **H-plane**
WG	$\pm 37°$	$\pm 17°$
RGW	$\pm 31°$	$\pm 39°$
WG + E-pl. grooves	$\pm 37°$	$\pm 28°$
RGW + E-pl. grooves	$\pm 47°$	$\pm 33°$
WG + E-/H-pl. grooves	$\pm 41°$	$\pm 26°$
RGW + E-/H-pl. grooves	$\pm 51°$	$\pm 50°$
RGW + AMC pins	$\pm 51°$	$\pm 60°$

with periodic boundary conditions (PBC) (details can be found in [8], [9], [11]). At the first study stage, the active reflection coefficient (Γ) was found versus frequency and scan angle for WG and RGW UCs with various decoupling structures; next, the mutual coupling coefficients of the corresponding array elements were calculated from the Γ results, where a post-processing approach is used to avoid a time-consuming simulation of a large-scale finite array fragment [12].

A. *Optimization of the Beam-Steering Performance*

The considered UCs include open-ended WG and RGW structures with variations of decoupling structures. The basic design concepts and some results were discussed in [8], [9]. In general, UCs were optimized to reach the largest beam-steering elevation angle (θ_{max}) through the criterion of $|\Gamma| \leq -10$ dB over the 20% relative bandwidth (85–105 GHz). The full-wave simulation results are summarized in Table. 1. Various configurations of the RGW array element are demonstrated in Fig.1, where the decoupling structures include E- and H-plane grooves [8], [9] [Fig.1(b),1(c)], and a bed of pins protruding over the UC aperture. The pins parameters are tuned to get the artificial magnetic conductor (AMC) surface response [see Fig.1(d)]. This way, the AMC structure realizes the surface wave bandgap region, i.e., a 2-D electromagnetic soft surface [13]. This technique has been widely used to suppress mutual coupling in wide-angle scanning printed PAAs [14]. The blue reference planes in Fig. 1 show where the decoupling structures start along z-axis. A detailed design description of the WG arrays can be found in [8].

Referring to Table 1, we can see that the standard WG UCs in the H-plane are limited by $\theta_{max} \leq 30°$ even with E-/H-plane grooves in the aperture, while the RGW UCs here typically demonstrate larger θ_{max} ($\geq 50°$). This is owing to a higher elements decoupling in both D- and H-plane of the RGW arrays (see below).

To further understand how the beam-steering performance is affected by various RGW element aperture modifications, in Fig. 2, we plotted $|\Gamma|$ maps in the full visible scan range for two selected frequencies. These results are discussed in connection with the post-processed mutual coupling coefficients in the following subsection.

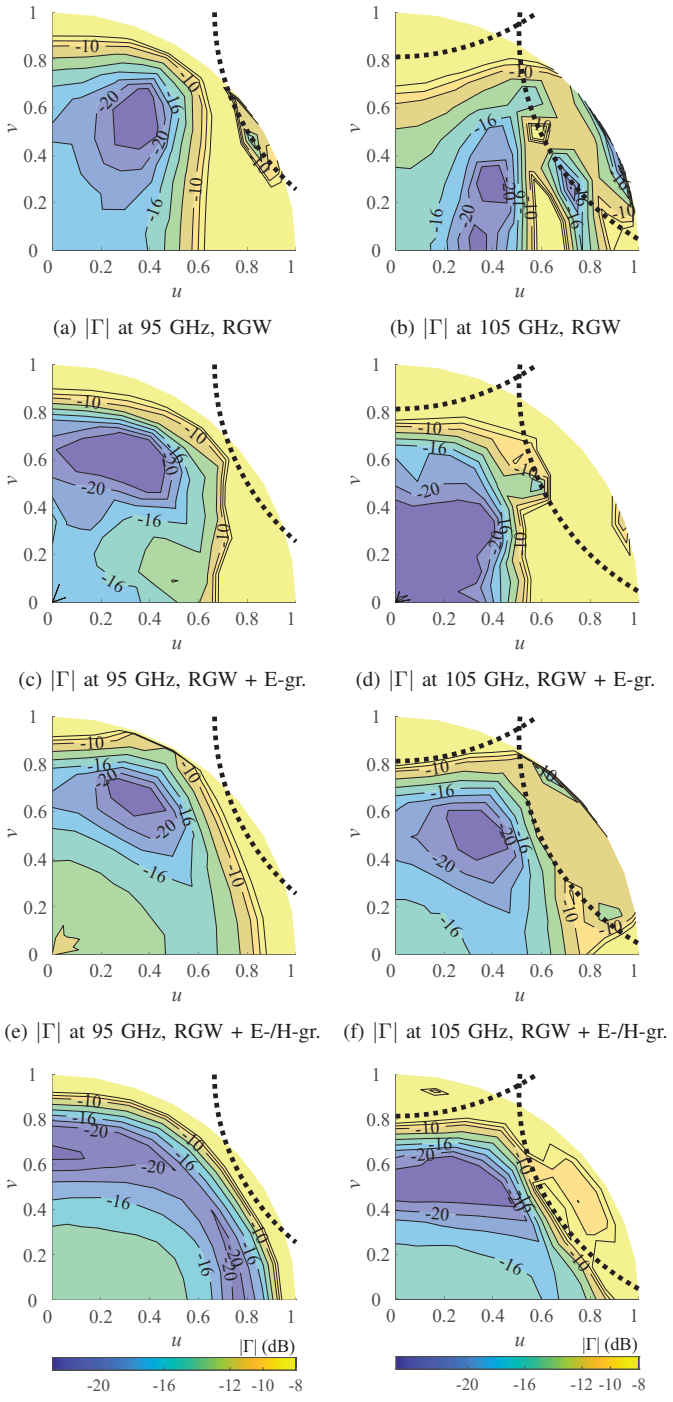

(a) $|\Gamma|$ at 95 GHz, RGW (b) $|\Gamma|$ at 105 GHz, RGW

(c) $|\Gamma|$ at 95 GHz, RGW + E-gr. (d) $|\Gamma|$ at 105 GHz, RGW + E-gr.

(e) $|\Gamma|$ at 95 GHz, RGW + E-/H-gr. (f) $|\Gamma|$ at 105 GHz, RGW + E-/H-gr.

(g) $|\Gamma|$ at 95 GHz, RGW + AMC pins (h) $|\Gamma|$ at 105 GHz, RGW + AMC pins

Fig. 2. Simulated active reflection coefficient (Γ) maps for the RGW elements with different decoupling aperture structures. Black dashed lines show grating lobe borders due to Floquet high-order modes ($m = -1, n = -1$ and $m = 0, n = -1$) propagation.

B. *Mutual Coupling Analysis*

A general view of the UC inside an infinite isosceles triangular array lattice is depicted in Fig. 3(a). The lattice geometry is shown in Fig. 3(b) with the reference element placed at the (0,0)-position. Here, the distances a and b represent the inter-element spacings in the H- and E-planes ($0.6\lambda_0$ and $0.5\lambda_0$, λ_0 – free-space wavelength at 95 GHz) respectively, which are the common parameters for all above-discussed UC designs. The array mutual coupling coefficients between the reference $(0, 0)$- and (i, j)-element

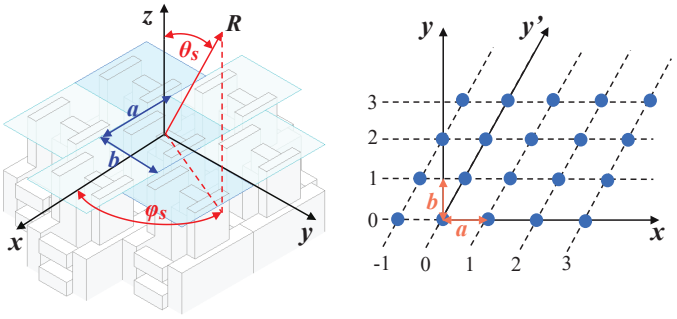

(a) (b)

Fig. 3. (a) The open-ended waveguide unit cell (the RGW element with E-[xz-plane] and H-plane [yz-plane] grooves is shown) in the array environment and (b) array isosceles triangular lattice configuration.

(S_{ij}) can be calculated using the 2-D Fourier series expansion of Γ, with S_{ij} representing the (i,j)-th Fourier coefficient in the $(\Psi_x, \Psi_{y'})$ phase space, where Ψ_x and $\Psi_{y'}$ represent the phase difference between adjacent elements along x- and y'-axis [Fig. 3(b)], i. e., $\Psi_x = 2\pi au/\lambda$, $\Psi_{y'} = 2\pi bv/\lambda + \Psi_x/2$ [11], [15]. Here, u and v are the scan direction cosines ($u = sin\theta_s cos\phi_s$, $v = sin\theta_s sin\phi_s$). Note that $\Psi_x, \Psi_{y'} \in [-\pi, \pi]$ that in general includes the invisible region of the (u, v) space.

To consider both accuracy and time-efficiency, the resolution of $\Delta\Psi_x = \Delta\Psi_{y'} = 6°$ was used in numerical integration, the results of which are shown in Fig. 4.

As Fig. 4(a) and 4(b) show, the RGW UC demonstrates lower $|S_{00}|$, but slightly higher coupling with the 3rd and 4th elements in the H-plane compared with the conventional WG. For $i \geq 5$, the $|S_{i0}|$ drops faster at higher frequencies for the RGW element. Overall, this results in the larger H-plane θ_{max} of the RGW element. When E-plane grooves are added to the WG/RGW UCs, coupling magnitudes show a significant reduction in the D-plane [$y'z$-plane, Fig. 3(b)]. This is correlated with the results observed in Fig. 2(a)-2(d) where Γ for the RGW element is significantly improved in the E- and D-planes (nearby the grating lobe borders) after adding the E-plane grooves. At the same time, the coupling level increases in the H-plane for both WG and RGW elements [see Fig. 4(c) and 4(d)]. However, it is surprising that the resulting H-plane θ_{max} has different trends for these elements, as $|\theta_{max}|$ increases from 17° to 28° for the WG element, and decreases from 39° to 33° for the RGW element. This interesting phenomenon is likely the result of a specific mutual coupling destructive superposition and should be investigated further.

When both the E- and H-plane grooves are added, the mutual coupling between elements becomes well-suppressed in both principal planes [Fig. 4(e)-4(f)]. However, the RGW element demonstrates a significantly larger H-plane scan range, which is likely due to a phase relation between S_{00} and S_{i0}. The RGW element performance improves further as the AMC pins are applied over the aperture: despite that the mutual coupling magnitudes are still very close to the grooved RGW element (see Fig. 4(f)-4(g)), its $|\Gamma| \leq -10$ dB range covers

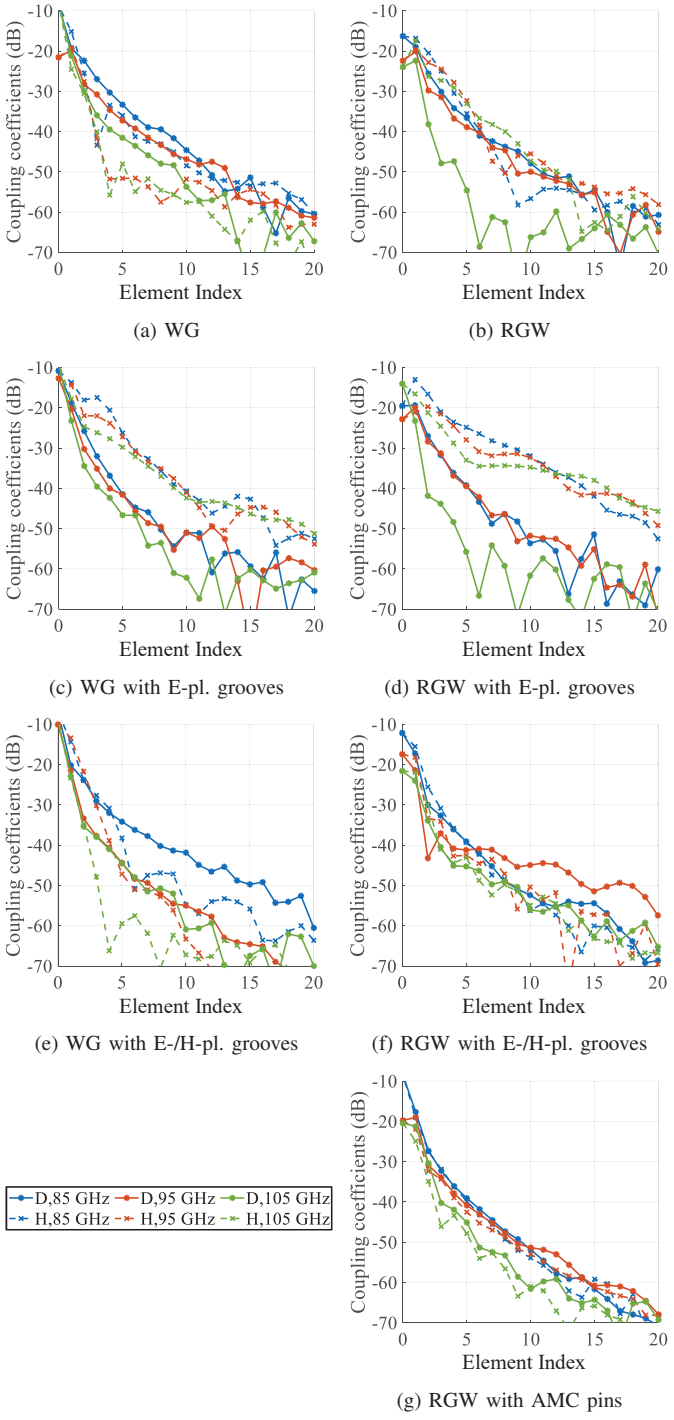

Fig. 4. Extracted coupling coefficient magnitudes in the D- and H-plane for various WG and RGW radiating elements in the infinite array environment. The elements numbering is given in Fig. 3(b).

almost all possible (u,v) values inside the grating-lobe-free visible region over all operating frequencies [see Fig. 2(h)]. The main improvement here is observed in the H-plane scanning range, which is the most noticeable at the high frequencies. To reveal the reason behind this, Fig. 5 gives a more comprehensive comparison of the mutual coupling

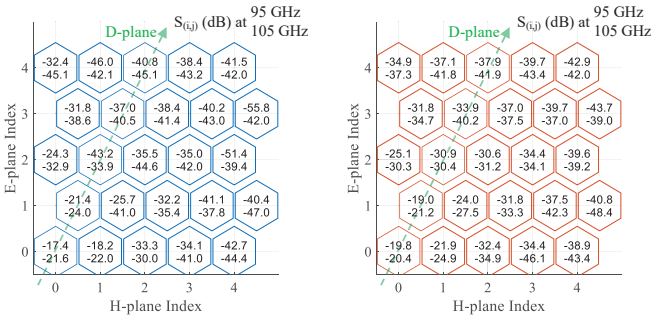

(a) RGW with E-/H-pl. grooves (b) RGW with AMC pins

Fig. 5. Extracted coupling coefficient magnitude maps for the central (0,0) and neighboring (i,j) RGW elements in the infinite array environment at 95 and 105 GHz.

magnitudes between several adjacent elements of two RGW arrays. The mutual coupling is, in general, well-suppressed for both arrays. However, we can see that in the H-plane of the AMC-loaded element the high-frequency suppression is more intense, which is the main reason for the extended H-plane scanning range.

III. Conclusion

In this paper, we analyzed the beam-steering performance of the open-ended ridge waveguide (WG) and ridge gap waveguide (RGW) array elements with the thorough investigation of the elements mutual coupling effects. Various decoupling structures were proposed to suppress the mutual coupling magnitude. The results evidence that the RGW elements with the grooved aperture perform larger H-plane scan angles ($\pm 50°$) over a relatively wide band ($\geq 20\%$) as compared with the conventional grooved WG elements. The latter improvement is not obvious since the H-plane coupling magnitudes for both element types are quite close. Therefore, it is believed that coupling phases could significantly contribute to the observed effect. Moreover, by adding the artificial magnetic conductor pins above the RGW element aperture, the further suppression of the mutual coupling level can be achieved that allows for the superior beam-steering range of $\pm 51°$ / $\pm 60°$ in the E- / H-plane over the $\geq 20\%$ (85-105 GHz) frequency bandwidth.

Acknowledgment

This work has received funding from the European Union's Horizon 2020 research and innovation programme under the Marie Skłodowska-Curie grant agreement No 860023 and the Sweden-Taiwan Collaborative Research Framework Project "Antenna Technologies for Beyond-5G Wireless Communication" from the Swedish Foundation for Strategic Research.

References

[1] T. S. Rappaport, Y. Xing, O. Kanhere, S. Ju, A. Madanayake, S. Mandal, A. Alkhateeb, and G. C. Trichopoulos, "Wireless communications and applications above 100 GHz: Opportunities and challenges for 6G and beyond," *IEEE Access*, no. 7, pp. 78 729–78 757, 2019.

[2] "European vision for the 6G network ecosystem," White Paper, The 5G Infrastructure Association, Jun. 2021.

[3] W. Shin, B.-H. Ku, O. Inac, Y.-C. Ou, and G. M. Rebeiz, "A 108–114 GHz 4× 4 wafer-scale phased array transmitter with high-efficiency on-chip antennas," *IEEE Journal of Solid-State Circuits*, vol. 48, no. 9, pp. 2041–2055, 2013.

[4] X. Gu, D. Liu, C. Baks, J.-O. Plouchart, W. Lee, and A. Valdes-Garcia, "An enhanced 64-element dual-polarization antenna array package for W-band communication and imaging applications," in *Proc. 2018 IEEE 68th Electronic Components and Technology Conference (ECTC)*, 2018, pp. 197–201.

[5] J. W. Jordan, S. Lynch, M. Clark, B. L. Cannon, L. A. Adames, D. Wrenn, K. Jackson, N. Erickson, J. Clough, D. Brown *et al.*, "Monolithically fabricated 4096-element, polystrata® broadband d-band array demonstrator," in *Proc. 2019 IEEE MTT-S International Microwave Symposium (IMS)*, 2019, pp. 1060–1063.

[6] B. L. Cannon, K. J. Vanhille, and G. A. Sadowy, "Microfabricated dual-polarized, W-band antenna architecture for scalable line arrav feed," in *2015 IEEE International Symposium on Antennas and Propagation & USNC/URSI National Radio Science Meeting*, 2015, pp. 615–616.

[7] A. Gomez-Torrent, M. Garcia-Vigueras, L. Le Coq, A. Mahmoud, M. Ettorre, R. Sauleau, and J. Oberhammer, "A low-profile and high-gain frequency beam steering subterahertz antenna enabled by silicon micromachining," *IEEE Trans. Antennas Propag.*, vol. 68, no. 2, pp. 672–682, 2020.

[8] Y. Zhang, A. R. Vilenskiy, and M. V. Ivashina, "W-band waveguide antenna elements for wideband and wide-scan array antenna applications for beyond 5G," in *Proc. 2021 15th European Conference on Antennas and Propagation (EuCAP)*, 2021, pp. 1–5.

[9] Y. Zhang, A. Vilenskiy, and M. Ivashina, "Wideband open-ended ridge gap waveguide antenna elements for 1-D and 2-D wide-angle scanning phased arrays at 100 GHz," *IEEE Antennas and Wireless Propagation Letters*, vol. 21, no. 5, pp. 883–887, 2022.

[10] A. Agrawal, M. Perry, and N. Landry, "Wideband ridge waveguide radiating element for phased array antennas," in *Proc. IEEE Antennas and Propagation Society International Symposium. 1995 Digest*, vol. 1, 1995, pp. 568–571.

[11] D. T. McGrath, "Calculation of coupling coefficients for arrays with skewed lattices from infinite array scan reflection data," *IEEE Transactions on Antennas and Propagation*, vol. 55, no. 7, pp. 2116–2119, 2007.

[12] A. K. Bhattacharyya, *Phased Array Antennas: Floquet Analysis, Synthesis, BFNs and active array systems*. Hoboken, NJ: John Wiley & Sons, 2006.

[13] P.-S. Kildal, "Three metamaterial-based gap waveguides between parallel metal plates for mm/submm waves," in *2009 3rd European Conference on Antennas and Propagation*, 2009, pp. 28–32.

[14] E. Adas, F. De Flaviis, and N. G. Alexopoulos, "Realization of scan blindness free finite microstrip phased arrays based on mode-free radiating electromagnetic bandgap materials," *IEEE Transactions on Antennas and Propagation*, vol. 66, no. 7, pp. 3375–3382, 2018.

[15] V. I. Litun, H. Rashid, and E. V. Komissarova, "Unit-cell versus finite array approaches for antenna array design," in *2021 Antennas Design and Measurement International Conference (ADMInC)*, 2021, pp. 23–26.